AUTOMATIC SEGMENTATION OF HEAD STRUCTURES ON FETAL MRI

Jérémie Anquez, Elsa D. Angelini, Isabelle Bloch

Institut TELECOM - Télécom ParisTech - CNRS UMR 5141 LTCI, Paris, France.

ABSTRACT

Recent improvements of fetal MRI acquisitions now allow three-dimensional segmentation of fetal structures, to extract biometrical measures for pregnancy follow-up. Automation of the segmentation process remains a difficult challenge, given the complexity of the fetal organs and their spatial organization. As a starting point, we propose in this paper a fully automated segmentation method to localize the eyes and segment the skull bone content (SBC). Priors, embedding contrast, morphological and biometrical information, are used to assist the segmentation process. A validation of the proposed segmentation method, on 24 MRI volumes of fetuses between 30 and 35 gestational weeks, demonstrated a high accuracy for eyes and SBC extraction.

Index Terms— Fetal imaging , MRI, eyes, skull, segmentation

1. INTRODUCTION

MRI constitutes a good adjunct to echography for pregnancy follow up [1]. Higher image quality and shorter acquisition times have led to an increase in the number of MRI exams performed. However, very few works have been dedicated to automatic segmentation of in utero fetal structures, except for brain segmentation [2, 3, 4] on data with field of views restricted to the fetal head.

Segmentations of other fetal structures are desirable to closely monitor fetal growth. As an example, a precise estimation of the fetus weight could be derived from biometrics measures, which is crucial when obstetricians need to plan for an optimal delivery procedure in case of fetal macrosomia (oversized fetuses). Using the Steady State Free Precession (SSFP) sequence, whole uterus MRI volumes can be acquired in less than 30 seconds, thus limiting imaging artefacts related to fetal motion. Moreover, the SSFP sequence provides adequate image quality for segmentation of fetal structures [5]. However, the MRI images contain complex information to process: (1) the SSFP sequence is highly sensitive to magnetic field inhomogeneity; (2) as a wide field of view is used, numerous maternal, uterine and fetal structures are visible; (3) the fetus orientation within the uterus (and hence with respect to the acquisition direction) is unknown. Our approach to process those images consists in identifying an initial structure in the fetal anatomy, to improve the knowledge of the fetal position and initialize the whole fetus segmentation process. Then, segmentation of neighboring organs can be performed sequentially in narrow regions of interest, using anatomical spatial relationships.

In this work, we use the eyes as initial structures, motivated by three factors: a fetal eye is small enough to be considered insensitive to image inhomogeneity, its spherical shape is rotationally invariant

and it highly contrasts with its surroundings. We propose an eye-extraction scheme based on template matching. By explicitly using the eyes localization, the neighboring skull bone content (SBC) is then segmented using a graph cut approach. Shape, contrast and biometrical priors are used to guide both segmentation tasks.

2. FETAL IMAGING AND PROBLEM OVERVIEW

A database containing 24 MRI volumes of fetuses between 30 and 35 gestational weeks was gathered. All the images were acquired with the SSFP sequence on two 1.5 Tesla superconducting units (Magnetom, Siemens©, Erlangen, Germany and Avanto, General Electric©, Milwaukee (WI), United States). Typical acquisition parameters were: TR/TE = 4.2/1.8 ms, flip angle = 60°, FOV = 480, slice thickness/gap = 4/0 mm, matrix = 512×512, while voxel size were 0.94 x 0.94 x 4 mm³. An MRI slice is shown in Figure 1, with the structures of interest (fetal eye and SBC) outlined respectively in green and red. The SBC includes the brain and the cerebrospinal fluid and is delimited by the boundary between the cerebrospinal fluid and the skull bone. Due to the T2-weighting component of the SSFP sequence, voxels intensity is strikingly higher in aqueous tissues than in fetal soft tissues and fetal bones. This explains why (1) the eye, which contains fluid-filled chambers, is brighter than the surrounding muscles and (2) the cerebrospinal fluid, which water content is about 99%, appears brighter than the skull bone.
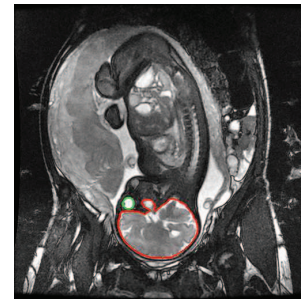
Fig. 1. 2D slice of an MRI volume I_k of the database. The eye is outlined in green and the SBC in red.

Figure 2 illustrates the different steps of the overall segmentation framework. (a) The eyes are detected in the whole image I_k using an appearance model. (b) The midsagittal slice M_k is reconstructed thanks to the eyes centers localization and the SBC is segmented, taking advantage of the closeness between the SBC and the eyes centers. (c) Orientation, position and scale information is extracted from the SBC segmentation in M_k, to perform a precise 3D segmentation.

Simple appearance models are built to guide the segmentation of fetal eyes and SBC. Contrast priors between those structures and their surroundings are embedded in the segmentation process, as

(a)   (b)   (c)
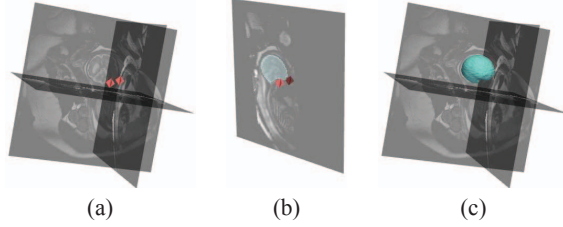
Fig. 2. Main steps of the proposed segmentation framework. (a) Eye detection in the image I_k. (b) Extraction of the midsagittal slice M_k using the eyes centers and 2D segmentation of the SBC. (c) 3D segmentation of the SBC using orientation, position and scale information extracted from 2D segmentation in M_k.

well as shape and biometrical priors. Those last two priors rely on information extracted through manual tracing on the image database. The eyes diameter d and the distance D between their centers E_1 and E_2 were measured, while the SBC was manually segmented to extract shape information.

    Considering the limited number of cases available in our database, the different steps of the proposed segmentation framework were validated using a leave-one-out cross validation procedure. When an image I_k is processed, a training database DB_k is considered. DB_k corresponds to the whole database, leaving I_k out.

3. EYES DETECTION

3.1. Eyes appearance modeling

Let μ_d and σ_d be the mean and the standard deviation of the eye diameter d on the database. We measured $\mu_d = 15.03$ mm and $\sigma_d = 0.74$ mm. Since σ_d is small (because the fetuses in our database are of similar gestational ages and do not exhibit any eye development pathology), the eye diameter is well modeled by using only μ_d. Considering the contrast and shape priors presented above, an eye template E is built, modeling the eye as a ball of diameter μ_d, brighter than the background. The typical image resolution in our database is $(r_x, r_y, r_z) = (0.94, 0.94, 4)$. r_z and μ_d are of the same order of magnitude and the eye is affected by partial volume effect as shown in Figure 3 (a,d). We propose to take into account these visual artefacts.

    A first isotropic template E' is considered at a resolution r' finer than r (Figure 3 (b,e)). Let v' be a voxel of E'. E' is then downsampled at the resolution r to obtain E (Figure 3 (c,f)). Let v be a voxel of E and V be the set of voxels v' contained in v. The partial volume effect being a mixture of multiple tissues inside a given voxel, we model the intensity of v as the mean intensity of the voxels belonging to V. This is an approximation of the actual MRI acquisition sampling process, but this is sufficient to generate a realistic template.

3.2. Eyes localization

A set of eye candidates $\{EC_i\}$ is computed using template matching. As a similarity measure, we use the normalized cross-correlation, which presents several advantages, such as being only sensitive to local contrast information. This is a key feature as the images obtained with the SSFP sequence are heterogeneous which can lead to great intensity variations in the eye and its surroundings from one image to another one. A normalized cross-correlation coefficients map ($N3C$) is computed using the template E, and then thresholded at a value t. Connected components are identified in the thresholded

(a)   (b)   (c)

(d)   (e)   (f)
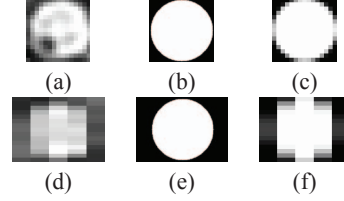
Fig. 3. Eye appearance model: central slices of an image I_k across one eye (a,d), E' (b,e) and E (c,f). (a,b,c) and (d,e,f) are slices in (X, Y) and in (X, Z) planes respectively. Image spatial resolutions are $r' = (0.1, 0.1, 0.1)$, for E', and $r = (0.94, 0.94, 4)$, for E and I, in millimeters.

map and one eye candidate $\{EC_i\}$ is extracted in each connected component, corresponding to the maximum of $N3C$ in the component. The threshold value t is extracted from the $N3C$ distribution considering all the images in the training database DB_k. With μ_{N3C} and σ_{N3C} the mean and standard deviation of $N3C$, we use $t = \mu_{N3C} + 2\sigma_{N3C}$.

(a)   (b)

(c)   (d)
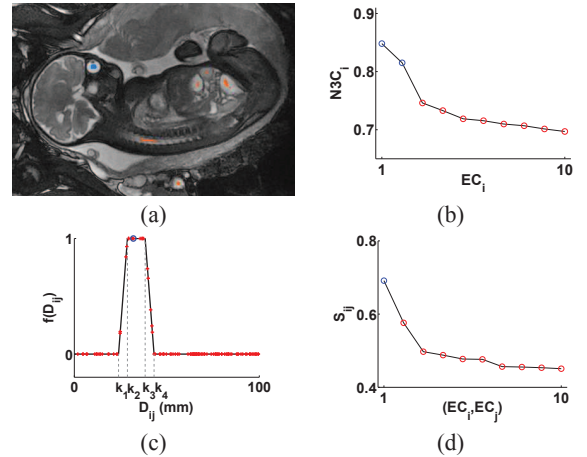
Fig. 4. Eye detection on an image I_k: (a) connected components extracted from the thresholded $N3C$ map, overlaid on a slice of I_k, (b) ten best EC_i, (c) membership function $f(D_{ij})$ and (d) ten best S_{ij}. The blue color identifies the results corresponding to the eye centers.

    All couples (EC_i, EC_j) of eye center candidates are then considered. The distance D_{ij} between EC_i and EC_j is computed and a soft selection is proposed to discard couples separated by inappropriate distance, building a trapezoid membership function f with keypoints (k_1, k_2, k_3, k_4). Using the mean μ_D and the standard deviation σ_D of the inter-eye distance D in DB_k, keypoints are defined as $(k_1, k_2, k_3, k_4) = (\mu_D - 4\sigma_D, \mu_D - 2\sigma_D, \mu_D + 2\sigma_D, \mu_D + 4\sigma_D)$. Combining conjunctively $f(D_{ij})$ with the $N3C$ values of EC_i and EC_j ($N3C_i$ and $N3C_j$) leads to the scoring function $S_{ij} = N3C_i.N3C_j.f(D_{ij})$, which is computed for every couple and identifies the couple with the highest score as the fetus eyes (E_1^*, E_2^*).

    Figure 4 shows intermediate results when applying the algorithm to an MRI volume I_k. On this image, $t = 0.53$ and 59 connected components were extracted from the thresholded $N3C$ map using this value, which remains reasonable. In (a), the connected components are plotted in a slice containing an eye center (blue component). The ten best EC_i are shown in (b), ordered by decreasing $N3C_i$. The best two correspond to the eyes centers (blue circles).

The selection function f, built with $\mu_D = 33.2$ mm and $\sigma_D = 2.4$ mm, is shown in black (c), along with the evaluation of the couples such that $D_{ij} < 100$. The couple corresponding to the eyes center returned 1 (blue circle) while 97.4% of the couples returned 0, demonstrating the high selectivity of f. Finally, (d) presents the ten best (EC_i, EC_j), ordered by decreasing S_{ij}. (E_1^*, E_2^*), corresponding to the highest S_{ij}, indeed matches the fetal eyes in the image.

For two MRI datasets I_k, the eyes centers did not correspond to the best two EC_i. However, the use of f discarded all false positives and the eyes centers were detected successfully on the whole database. The average discrepancy between the eyes centers E_i^* provided by the algorithm and those manually localized E_i, $i \in \{1, 2\}$, was 1.7 mm and a precise detection was hence performed.

4. SKULL BONE CONTENT SEGMENTATION

4.1. Skull bone content modeling

We now consider the SBC, defined as the volume delimited by the boundary between the skull bone and the cerebrospinal fluid. Several factors prevent the use of an appearance model, as was done for the eyes, for the SBC segmentation. First, important changes affect the fetal brain during the gyration phase, which occurs from the 28th to 35th gestational week and therefore concerns the fetuses in our database. During this phase, the SBC presents variable visual characteristics. Moreover, the fetal head surroundings can include different maternal and uterine structures, depending on the fetal position. Finally, given the SBC size, field inhomogeneities make the intensity of the SBC structures variable and cannot be neglected. Hence, a different approach is adopted and an average shape model is built using the SBC manual segmentations. Leaving I_k out, binary segmented shapes in DB_k are registered using a similitude transform and averaged in order to derive a mean shape model of SBC denoted SM. Figure 5 illustrates one SM. It is important to point out here that the different SM are very similar, showing a weak sensitivity to the I_k left out of the training set. Therefore, any SM could be used to process a new image added to the database.
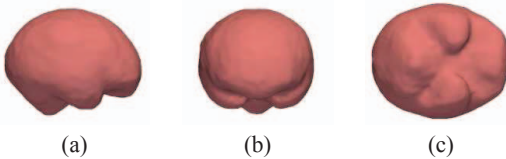
Fig. 5. 3D mean shape model SM. (a) Right, (b) anterior and (c) inferior views.

SM and a contrast prior between the cerebrospinal fluid and the skull bone are combined in a segmentation process involving two steps. Firstly, the midsagittal slice M_k is extracted using (E_1^*, E_2^*) and the SBC is segmented in this slice, to fully determine the fetal head orientation and initialize the 3D segmentation of the SBC. Indeed, E_1^* and E_2^* define the lateral orientation of the fetal head, but anterior-posterior and inferior-superior orientations are unknown. Secondly, the 2D segmentation of SBC is used to precisely embed the shape model SM in the 3D data, and perform a narrow-band 3D segmentation of the SBC.

4.2. Skull bone content segmentation in the midsagittal slice

Let $\bar{E}$ be the center of the $[E_1^* E_2^*]$ segment. The midsagittal slice M_k, passing through $\bar{E}$ and orthogonal to $\overrightarrow{E_1^* E_2^*}$, is reconstructed. Let SM_{2D} denote the 2D mean shape model of SBC corresponding

to the midsagittal slice of SM. For different locations and orientations of SM_{2D}, a segmentation is performed in a narrow-band, providing different SBC candidates. The best one is then selected as the most similar to SM_{2D}. The details of the method are as follows.

SM_{2D} is translated in order to be at a proper distance from $\bar{E}$, and L orientations of SM_{2D} are considered, rotating SM_{2D} around $\bar{E}$ with angles $\theta^l = (l 2\pi)/L$, $l \in [0, L-1[$. Let SM_{2D}^l be SM_{2D} rotated with the angle θ^l. SM_{2D}^l is eroded and dilated to provide two objects $\epsilon(SM_{2D}^l)$ and $\delta(SM_{2D}^l)$, which are used to define a narrow-band $NB^l = \delta(SM_{2D}^l) \backslash \epsilon(SM_{2D}^l)$. A graph cut segmentation is performed in NB^l [6]. Oriented edges are created between neighboring pixels. Two special nodes, the source S and the sink T, are added. Edges are created between (1) S and the pixels of NB^l adjacent to $\epsilon(SM_{2D}^l)$ and (2) T and the pixels of NB^l adjacent to $\delta(SM_{2D}^l)$. The minimal cut of the graph provides a binary segmentation corresponding to a minimal path in the region located between the source and the sink, considering the edge weights. Let p and q be two neighboring pixels and I_p and I_q their intensity. The weight of the edge linking p to q is defined as $w_{pq} = e^{-(I_p - I_q)^2/2\sigma^2}$, if $I_p > I_q$, and $w_{pq} = 1$, if $I_p \leq I_q$. This weighting includes contrast prior [7]. As the cerebrospinal fluid is brighter than the skull bone, edges linking cerebrospinal fluid pixels to skull bone pixels have a low weight. Thus, those edges are prone to belong to the minimal cut. The segmentation result provides the brain candidate SBC_{2D}^l in the position l. The similarity between the brain candidates shape and the shape model is evaluated by computing the kappa measure κ^l between SBC_{2D}^l and SM_{2D}^l for each orientation. The final SBC_{2D} segmentation result, denoted by SBC_{2D}^*, corresponds to SBC_{2D}^l for which κ^l is maximum.
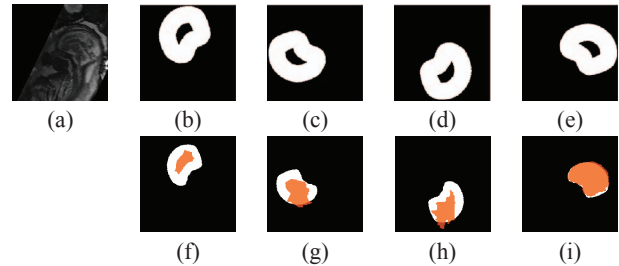
Fig. 6. SBC segmentation in 2D. (a) A midsagittal slice M_k. (b,c,d,e) The narrow-bands NB^l and (f,g,h,i) the brain candidates SBC_{2D}^l (orange) segmented in NB^l, overlayed on the rotated shape model SM_{2D}^l, for $\theta_l \in \{0, \pi/2, \pi, 3\pi/2\}$.

We have used $L = 24$ rotation steps and $\sigma = 4$ in all the experiments. The erosion and dilation radius used to generate NB^l (R_e and R_d respectively) are learned from DB_k, using manual segmentations of the SBC_{2D}, denoted SBC_{2D}^{man}. Let r_e and r_d be the minimum erosion and dilation radius garanteeing that there exists an $l_0 \in L$ such that $\epsilon(SM_{2D}^{l_0}) \subset SBC_{2D}^{man}$ and $SBC_{2D}^{man} \subset \delta(SM_{2D}^{l_0})$ for any element of DB_k. We ended up using $R_e = 0.5 r_e$ and $R_d = 1.5 r_d$, to tolerate SBC_{2D} to segment to be smaller or bigger than all SBC_{2D} represented in DB_k and to ensure that boundaries are included in a given NB^l.

Figure 6 presents the midsagittal slice M_k from one dataset and intermediate results for $\theta_l \in \{0, \pi/2, \pi, 3\pi/2\}$. For this image $R_e = 20$, $R_d = 18$. Figure 7 plots κ^l values for all θ_l. The highest κ^l was obtained for $\theta_l = 3\pi/2$ and SBC^l shown in Figure 6 (i) corresponded to SBC_{2D}^*. For each element of the database, the mean distance, the kappa measure and the Hausdorff distance were computed between SBC_{2D}^* and SBC_{2D}^{man}. The mean values on the

whole database for each indicator are noted μ_{md}, μ_κ and μ_{hd} respectively. We obtained $\mu_{md} = 0.7$ mm, $\mu_\kappa = 0.98$ and $\mu_{hd} = 3.9$ mm, providing a very good agreement between manual and automatic segmentations of SBC in M_k.
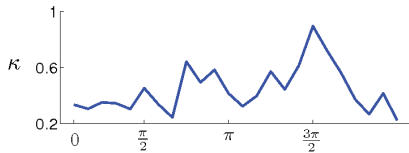
Fig. 7. Values of κ^l depending on θ_l ($L = 24$). The highest score is obtained for $\theta_l = 3\pi/2$. See Figure 6 (i) for the corresponding result.

4.3. Skull bone content segmentation in 3D

SM is first scaled using the areas ratio between SBC^*_{2D} and SM_{2D}, before being embedded in I_k using the centroid and the principal directions of SBC^* as shown in Figure 2 (c). The registered SM is noted $T(SM)$. An algorithm similar to the one used for the SBC detection in M_k is used. $T(SM)$ is eroded and dilated to provide two objects $\epsilon(T(SM))$ and $\delta(T(SM))$ in order to build the narrow-band $NB = \delta(T(SM))\backslash\epsilon(T(SM))$. A graph cut segmentation is performed in NB, the graph being built as explained in Section 4.2, considering 3D neighborhoods and weights w_{pq} including the distance between voxels. We set $w_{pq} = e^{-(I_p-I_q)^2/2\sigma^2}/dist(p,q)$, if $I_p > I_q$, and $w_{pq} = 1/dist(p,q)$ if $I_p \leq I_q$.

The mean kappa measure between the SBC manual segmentation SBC^{man} and $T(SM)$ was 93% on the database. This high accuracy of the registration process derives directly from the good quality of the SBC segmentation in M_k. The erosion and dilation radiuses used to generate NB are learned from DB_k using the approach presented in Section 4.2. $T(SM)$ being close to the SBC boundaries, small radiuses are considered. Hence, a very constrained NB is defined which is crucial to obtain a correct segmentation of the SBC. As a matter of fact, partial volume effect degrades SBC boundaries on some slices, thus lowering the contrast between the cerebrospinal fluid and the skull bone. When a wide SR is considered, preliminary tests have shown some leakage in the segmentation result due to weak contrast.

The kappa measure between the manual segmentation SBC^{man} and the segmentation result has been evaluated for different σ values. Similar results were obtained for $\sigma \in [2, 5]$ showing the robustness of the algorithm. The mean value of the mean distance μ_{md}, the kappa measure μ_κ and the Hausdorff distance μ_{hd} were computed between the segmentation result and SBC^{man} considering the whole database. High precision segmentations were obtained: $\mu_{md} = 0.5$ mm, $\mu_\kappa = 0.98$ and $\mu_{hd} = 3.4$ mm. Figure 8 presents the SBC segmentation result in orthogonal views for one I_k.

5. CONCLUSION

A fully automatic method is proposed to segment the skull bone content on fetal MRI. The fetal eyes are first localized using a template combining contrast, shape and biometric priors. Based on the eyes localization, the midsagittal plane M_k is reconstructed and the SBC is segmented in M_k. This intermediate 2D segmentation result is used to embed a SBC shape model in the 3D data, in order to segment the structure in a restricted region. The segmentation is performed using a graph cut approach on a graph exploiting contrast priors. Precise segmentation results were obtained on 24 fetal MRI
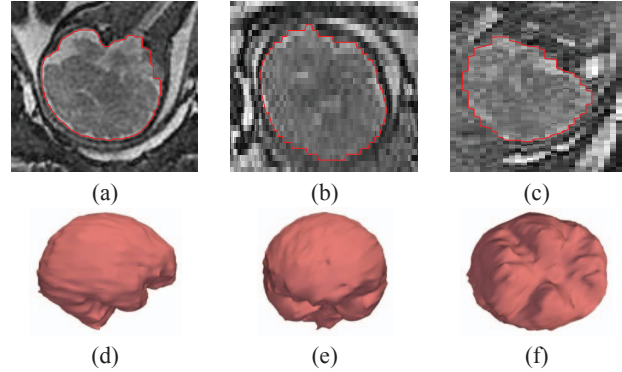
Fig. 8. 2D slices and SBC boundary in (X,Y) (a), (X,Z) (b) and (Y,Z) (c). 3D reconstruction of the segmentation in right (d), anterior (e) and inferior (f) views.

cases, which can be used for morphological and biometrical analysis of the fetal SBC. The whole segmentation process takes less than 5 minutes on a 3.5 GHz PC running MATLAB (The MathWorks Inc.).

The method is applied on images on which the fetus orientation is unknown. The fetal eyes localization and the SBC segmentation provide information on the fetus head orientation. Benefiting from the detection of the fetal spine root in the SBC, the segmentation of the fetus spine is now in progress, in order to increase the knowledge on the fetus trunk orientation and size. Further works will include a segmentation of the brain in the SBC to extract morphological, biometrical and maturation information.

6. REFERENCES

[1] D. Prayer and P.C. Brugger, "Investigation of normal organ development with fetal MRI," *European Radiology*, vol. 17, no. 10, pp. 2458–2471, 2007.

[2] A. Cachia, J.F. Mangin, D. Riviere, F. Kherif, N. Boddaert, A. Andrade, D. Papadopoulos-Orfanos, J.B. Poline, I. Bloch, M. Zilbovicius, et al., "A primal sketch of the cortex mean curvature: a morphogenesis based approach to study the variability of the folding patterns," *IEEE Transactions on Medical Imaging*, vol. 22, no. 6, pp. 754–765, 2003.

[3] I. Claude, J.L. Daire, and G. Sebag, "Fetal brain MRI: segmentation and biometric analysis of the posterior fossa," *IEEE Transactions on Biomedical Engineering*, vol. 51, no. 4, pp. 617–626, 2004.

[4] P.A. Habas, K. Kim, F. Rousseau, O.A. Glenn, A.J. Barkovich, and C. Studholme, "Atlas-based segmentation of the germinal matrix from in utero clinical MRI of the fetal brain.," in *International Conference on Medical Image Computing and Computer-Assisted Intervention*, 2008, vol. 11, pp. 351–358.

[5] J. Anquez, E. Angelini, I. Bloch, V. Merzoug, A. E. Bellaiche-Millischer, and C. Adamsbaum, "Interest of the Steady State Free Precession (SSFP) sequence for 3D modeling of the whole fetus," in *Engineering in Medicine and Biology Conference*, 2007, pp. 771–774.

[6] Y. Boykov, O. Veksler, and R. Zabih, "Fast Approximate Energy Minimization via Graph Cuts," *IEEE Transactions on Pattern Analysis and Machine Intelligence*, pp. 1222–1239, 2001.

[7] Y. Boykov and G. Funka-Lea, "Graph Cuts and Efficient NDImage Segmentation," *International Journal of Computer Vision*, vol. 70, no. 2, pp. 109–131, 2006.